The influence of metal cations on the dissolution and transformation of biotite

Shoushu Wei[a, b, c], Qingze Chen[a, b, c], Lingya Ma[a, b, c], Xiangwei Zhang[a, b, c], Jingming Wei[a, b, c], Jiaxin Xi [a, b, c], Runliang Zhu[a, b, c], Jianxi Zhu[a, b, c]*, Hongping He[a, b, c]

[a] *CAS Key Laboratory of Mineralogy and Metallogeny, Guangdong Provincial Key Laboratory of Mineral Physics and Materials, Guangzhou Institute of Geochemistry, Chinese Academy of Sciences, Guangzhou 510640, China*

[b] *CAS Center for Excellence in Deep Earth Science, Guangzhou 510640, China*

[c] *University of Chinese Academy of Sciences, Beijing 100049, China*

* Corresponding author

E-mail: zhujx@gig.ac.cn

This is a 'preproof' accepted article for Mineralogical Magazine. This version may be subject to change during the production process.
DOI: 10.1180/mgm.2024.67

ABSTRACT

Five typical metal cations (*i.e.*, Na^+, K^+, Ca^{2+}, Mg^{2+}, Al^{3+}) were selected as representatives to study the influence of metal cations on the dissolution and transformation of biotite. This work focused on the mineralogical features of transformation products and the phase transformation mechanisms by utilizing modern spectroscopic methods and micro-beam characterization techniques. In comparison to the control system, K^+ inhibited the dissolution and transformation of biotite, leading to the generation of amorphous iron hydroxides on the biotite surface. Na^+, Mg^{2+}, and Ca^{2+} promoted the dissolution of biotite but inhibited its transformation into kaolinite, with the Na system producing sodium-bearing biotite, vermiculite, hematite, and a small amount of kaolinite, and the Mg and Ca systems producing mainly vermiculite, chlorite, and hematite. Al^{3+} notably accelerated the dissolution and transformation of biotite, resulting in well-crystallized kaolinite and hematite. Furthermore, metal cations changed the formation mechanism of kaolinite by altering the dissolution rate of biotite. Within the blank system, biotite dissolved slowly, with elements (*i.e.*, Al and Si) accumulating on the biotite surface and growing epitaxially into kaolinite; while in the Al system, the rapid dissolution of biotite provided a large amount of Si, which combined with Al in the solution, forming kaolinite *via* a dissolution-recrystallization process. In addition, the exchange reactions of metal cation-K^+ and the competitive adsorption of metal cation-proton simultaneously constrained the dissolution process of biotite. This work offered a theoretical basis for an in-depth comprehension of the factors influencing biotite weathering and new insights into the evolution of clay minerals in terrestrial surface environments.

***Keywords*:** Biotite, metal cation, dissolution, transformation, weathering.

https://doi.org/10.1180/mgm.2024.67 Published online by Cambridge University Press

Introduction

Biotite is a typical 2:1 phyllosilicate mineral, constituting approximately 8% of the Earth's crust mass (Nesbitt and Young, 1984). Influenced by the chemical weathering of surface water and microbial activities, biotite undergoes dissolution and transformation, giving rise to secondary minerals, such as hydrobiotite, vermiculite, and kaolinite (McMaster *et al.*, 2008; Galán and Ferrell, 2013; Wu *et al.*, 2023), which are significant parts of soil minerals. Moreover, the K^+ within the interlayer of biotite is gradually exchanged by H^+ or other hydrated metal cations, often accompanied by the oxidation of octahedral Fe^{2+} and dissolution of other cations (Bray *et al.*, 2015; Lamarca-Irisarri *et al.*, 2019; Wang *et al.*, 2024). The released elements, such as K, Mg, and Fe, serve as crucial nutrients for the biosphere (Bowser and Jones, 2002; Samantray *et al.*, 2022). Additionally, biotite weathering consumes CO_2, acting as a net sink in the global carbon cycle, thereby influencing global climate (Wilson, 2004; Van Der Kellen *et al.*, 2022). As such, biotite weathering impacts geochemical processes such as soil formation, elemental migration and enrichment, nutrient supply to the biosphere, and the overall carbon balance on Earth.

The dissolution and transformation of biotite are key processes in biotite weathering, which have been proven to be strongly influenced by environmental conditions. For instance, under acidic conditions, a higher concentration of H^+ (*i.e.*, lower solution pH) results in an accelerated biotite weathering rate (Pachana *et al.*, 2012; Cappelli *et al.*, 2023; Holgersson *et al.*, 2024). Furthermore, organic acids facilitate mineral dissolution by complexing with metal ions on the mineral surface (Ganor *et al.*, 2009; Haward *et al.*, 2011). On the other hand, inorganic cations are widely distributed in the surface environment (*e.g.*, soil and groundwater) with various types (*e.g.*, Ca^{2+}, Mg^{2+}, Na^+, and K^+)

https://doi.org/10.1180/mgm.2024.67 Published online by Cambridge University Press

and large concentration variations (ranging from μM to M levels) (Breen *et al.*, 1985; Kharaka and Hanor, 2014), which also have a non-negligible influence on biotite weathering. For example, in experiments simulating the effects of cations on biotite weathering, Na^+, Rb^+, and Cs^+, due to their identical charge and comparable radius to K^+, could significantly enhance the release of interlayer K^+ in biotite (Kim and Kim, 2015; Wang *et al.*, 2023). Among them, hydrated Na^+ entered the interlayer of biotite and opened the interlayer channels, promoting the dissolution of the layer structures (Kim and Kim, 2015). Min *et al.* (2018) studied how Na^+ and K^+ impact the dissolution/transformation of biotite under acidic hydrothermal conditions. They found that even a small amount of K^+ in the solution could inhibit biotite dissolution. A low concentration of Na^+ (less than 0.5 mol/L) could promote biotite dissolution, while the promoting effect of a high concentration of Na^+ (greater than 0.5 mol/L) was reduced, which was attributed to the competitive interaction between Na^+ and protons. Moreover, in the presence of Na^+, noticeable cracks appeared on the surface of the reacted biotite, and fibrous illite was formed (Hu *et al.*, 2011). Therefore, metal cations have a great impact on the dissolution process and transformation products of biotite.

Previous research has primarily concentrated on the influence of a certain type of cation (mostly alkali metal cations) on biotite dissolution. However, there are various cations in the terrestrial environment, with significant differences in their properties (*e.g.*, valence, ionic radius, and hydration capacity, Table S1) (Teppen and Miller, 2006; Tansel, 2012), which differ in their affinity for biotite. Further research is needed to clarify the influence of the type of cation on the dissolution and transformation of biotite. On the other hand, in the current studies on the interaction between cations and biotite, the emphasis is

https://doi.org/10.1180/mgm.2024.67 Published online by Cambridge University Press

generally on the impact of cations on the dissolution kinetics and mechanisms of biotite, with insufficient research on the accompanying phase transformation process of biotite.

In this work, five typical metal cations (Na^+, K^+, Ca^{2+}, Mg^{2+}, Al^{3+}) were selected as representatives to study the effect of cation types on the dissolution and transformation of biotite. By combining modern spectroscopic methods and micro-beam characterization techniques, we focused on the mineralogical characteristics of the transformation products (*e.g.*, phase composition, microstructure, and surface morphology) and the relevant phase transformation mechanisms. This work sought to clarify the influence of metal cation types on the dissolution and transformation of biotite, providing new information for an in-depth understanding of biotite weathering in the surface environment.

Experimental section

Materials

The pristine biotite (Bt) from Hebei, China, was initially purified through manual selection, light cleaning, and magnetic separation. Subsequently, the material was ground into a powder and passed through a 200-mesh sieve, with the undersized particles being reserved for further experiments. The structural chemical formula of biotite was calculated to be $(K_{0.87}Na_{0.04}Ca_{0.02})(Mg_{1.69}Mn_{0.01}Fe_{0.92}Ti_{0.10}Al_{0.17})(Al_{1.25}Si_{2.75})O_{10}(F_{0.06}(OH)_{0.92})_2$ according to the corresponding chemical composition (Table S2). Sodium chloride (NaCl), potassium chloride (KCl), magnesium chloride ($MgCl_2$), calcium chloride ($CaCl_2$), aluminum chloride hexahydrate ($AlCl_3 \cdot 6H_2O$), and hydrochloric acid (HCl, 37 wt.%) were all procured from Guangzhou Chemical Reagent Factory.

https://doi.org/10.1180/mgm.2024.67 Published online by Cambridge University Press

Dissolution experiments

First, solutions of NaCl, KCl, $CaCl_2$, $MgCl_2$, and $AlCl_3 \cdot 6H_2O$ with concentrations of 0.60 mol/L were prepared, and the system pH was set to 2 by adding an HCl solution. 50 mL of the above solutions were placed in different reaction vessels (with PTFE liners), followed by adding 0.10 g of biotite. Subsequently, the sealed reaction vessels were transferred to an oven at 150°C to initiate the dissolution/transformation experiment of biotite. The solution pH and reaction temperature settings were designed to accelerate the reaction rate (Cho and Komarneni, 2007; Lamarca-Irisarri *et al.*, 2019). Sampling was done at set time points (0 to 90 d), and the post-reaction suspension was centrifuged to collect the supernatant. The concentrations of various cations in the solution were analyzed utilizing a Thermo iCAP 7000 series inductively coupled plasma-atomic emission spectrometry (ICP-AES). The solid products were washed with distilled water, air-dried at room temperature, and collected for structural and morphological analysis. Based on the type of cation used and the reaction time, the resulting products were labeled as Bt-*M*-*y*d (where *M* represents the cation type and *y* denotes the sampling days). For instance, Bt-Na-30d signified the product obtained after biotite reacted for 30 days in the NaCl solution. Additionally, the control experiment (blank system) where no cations were added, but all other conditions remained consistent with the above experiment, resulted in products labeled as Bt-H-*y*d (with *y* representing the sampling days). For brevity, the systems containing NaCl, KCl, $CaCl_2$, $MgCl_2$, and $AlCl_3 \cdot 6H_2O$ solutions were abbreviated as the Na system, K system, Ca system, Mg system, and Al system, respectively.

https://doi.org/10.1180/mgm.2024.67 Published online by Cambridge University Press

Characterization Methods

Powder X-ray diffraction (XRD) patterns were determined utilizing a Bruker AXS D8 ADVANCE X-ray diffractometer fitted with Ni-filtered CuKα radiation (λ = 1.541 Å) at 40 kV and 40 mA. The powdered samples were loaded into the holder and flattened with a glass slide for measurement.

Thermogravimetric (TG) curves were recorded using a NETZSCH STA 409PC synchronous thermal analyzer. The sample was heated in a corundum crucible from 30°C to 1000°C under a N_2 flow (60 ml min^{-1}) with a ramp rate of 10°C min^{-1}. The derivative thermogravimetry (DTG) curve was generated by differentiating the TG curve.

Fourier transform infrared spectroscopy (FTIR) analysis was conducted using a Bruker Vertex-70 FTIR spectrometer. The mixture of KBr powder and the sample with a mass ratio of 80:0.9 was pressed into molds to form thin sheets for measurement. The spectra were collected over a range of 400 to 4000 cm^{-1}.

^{57}Fe Mössbauer spectra were obtained at room temperature through transmission mode, employing a Silver Double Limited WSS-10 Mössbauer spectroscopy system with a ^{57}Co/Rh as the Mössbauer source. The velocity-driven sensor functioned in a triangular wave mode within the energy range of ±15 mm/s, and the acquired spectra were performed using MossWinn 4.0 software.

Transmission electron microscopy (TEM) images, high-angle annular dark-field (HAADF) images, and energy-dispersive X-ray spectroscopy (EDS) were obtained using a FEI Talos F200S field-emission transmission electron microscope operating at 200 kV. The sample powder underwent ultrasonic dispersion in anhydrous ethanol, after which a drop of the suspension was deposited on a carbon-coated copper grid and allowed to air-

https://doi.org/10.1180/mgm.2024.67 Published online by Cambridge University Press

dry before observation. To capture high-resolution transmission electron microscopy (HRTEM) images, a minute sample portion was embedded within an epoxy matrix, cured by heating, and then sliced into thin sections (~75 nm thick) using the Leica EM UC7 ultramicrotome. These sliced samples were picked up with a copper grid for observation.

Results and discussion

Effect of various cations on biotite dissolution

To study the influence of cation types on biotite dissolution, the ion concentrations of K, Fe, and Si in the supernatant of different cation systems after 30 d of dissolution experiments were measured. The concentrations of these three elements in the solution can respectively indicate the dissolution of interlayer ions, tetrahedral sheets, and octahedral sheets of biotite. The ion concentrations, normalized by the stoichiometry of biotite, revealed that the K concentration in the Na, Mg, and Ca systems' solution was notably higher than in the blank system (Fig. 1a), due to the promotion of interlayer ion exchange of biotite by the metal cations. However, these three systems exhibited no Fe and a lower concentration of Si in the solution compared to the blank system (Fig. 1b and c). On the other hand, the solution pH values (3.50-4.00) of the Na, Mg, and Ca systems after reactions were higher than that of the blank system (2.53) (Table S3), indicating that more protons were consumed in the cation systems (leading to more intense dissolution of biotite). Hu *et al.* (2013) found through atomic force microscopy that when large-radius hydrated cations entered the interlayer of biotite *via* ion exchange, the biotite layer underwent significant swelling, which promoted layer bulging and crack formation, and thus increased the chance of proton attack on the layers. In this study, the dissolution of

https://doi.org/10.1180/mgm.2024.67 Published online by Cambridge University Press

structural Fe and Si from biotite was expected to be greater in the cation systems compared to the blank system. However, the enhanced dissolution of biotite consumed more protons, and the raised solution pH caused the dissolved Fe to precipitate in the form of hydroxides, hence Fe was almost undetectable in the solution of the cation systems (Fig. 1b). Additionally, the weakly crystalline iron hydroxides formed had a strong adsorption capacity for silicate ions (Carlson and Schwertmann, 1981; Hiemstra, 2018), adsorbing a certain amount of released Si (resulting from the structural degradation of biotite). This led to a lower Si concentration in the cation system. The low Fe content in the solution of the blank system could be linked to the adsorption effect of clay minerals (*e.g.*, hydrobiotite and vermiculite, confirmed by the XRD and TEM later) formed during the dissolution and transformation of biotite.

Compared with the blank system, the K system showed lower concentrations of Fe and Si (Fig. 1b and c) and a smaller increase in solution pH after the reaction (Table S3), indicating a lower dissolution degree of biotite in this system. This phenomenon was primarily due to the competitive interaction between K and protons on the biotite surface, leading to a reduced proton attack on the layers. Owing to the hindered dissolution of biotite and the substantial amount of added K^+, the alteration in K^+ concentration within the solution of the K system resulting from the cation exchange reaction was barely discernible. In the Al system, the K concentration in the solution was comparable to that in the Na, Mg, and Ca systems (Fig. 1a), but the concentrations of structural Fe and Si greatly increased (Fig. 1b and c), and the solution pH after the reaction (2.63) was close to that of the blank system (Table S3). This was because the hydrolysis of added Al^{3+} generated a large number of protons (Cho and Komarneni, 2007; Li *et al.*, 2020), significantly promoting the

https://doi.org/10.1180/mgm.2024.67 Published online by Cambridge University Press

dissolution of biotite while preventing a substantial increase in solution pH.

In all the systems, the normalized ion concentrations of K, Si, and Fe were asynchronous, indicating a non-stoichiometric dissolution behavior of biotite. Among them, the normalized ion concentration of K was the highest, followed by Si, and Fe was the lowest (except for the Al system). It was generally believed that under acidic conditions, the dissolution of biotite structural ions was mainly influenced by protons, with octahedral cations such as Mg and Fe dissolving first, followed by tetrahedral Al, and finally Si. This sequence was attributed to the weaker chemical bonds of Fe/Mg-O in the octahedral sheets compared to Al/Si-O in the tetrahedral sheets (Bray *et al.*, 2015; Masson *et al.*, 2024). The normalized ion concentration of Fe in the solution was lower than that of Si in this work, due to the adsorption of dissolved Fe by secondary products (such as clay minerals) (Jolicoeur *et al.*, 2000) and the formation of iron hydroxides (Tamrat *et al.*, 2018). The non-stoichiometric dissolution of various elements in biotite has been frequently reported in previous studies (Kalinowski and Schweda, 1996; Bray *et al.*, 2015; Holgersson *et al.*, 2024). In contrast to the aforementioned systems, the normalized ion concentration of Fe was higher than that of Si in the Al system, as the dissolved Si reacted with Al in the solution to form kaolinite (verified by the phase analysis of the biotite-transformed products below).

Structure of biotite-transformed products in various cation systems

XRD analysis

XRD patterns of the resulting products following the dissolution reaction of biotite for a certain period in various cation systems were recorded (Fig. 2). The XRD pattern of the original Bt exhibited sharp characteristic reflections of biotite, without any other phase

https://doi.org/10.1180/mgm.2024.67 Published online by Cambridge University Press

signals (Jeong and Kim, 2003) (Fig. 2a), indicating the sample's high purity. For the blank system, the XRD pattern of the product at 30 d showed the characteristic reflections of vermiculite, chlorite, and hydrobiotite, while still retaining relatively distinct reflections of biotite (Fig. 2a). Hydrobiotite belonged to a 2:1 regular interlayer clay mineral, with a structure formed by alternating vermiculite layers and biotite layers in a 1:1 arrangement. The products in the Na system exhibited a similar phase composition to the blank system but with stronger reflections of vermiculite and weaker reflections of the original biotite, indicating a higher reaction rate of biotite. According to ion concentration analysis, Na^+ could promote the exchange of K^+ within the interlayer of biotite. Na^+ with a larger hydration capacity than K^+ entered the interlayer space from the layer edges, opened the interlayer channels, and allowed more protons to enter the interlayers, facilitating the dissolution of structural ions (Sánchez-Pastor *et al.*, 2010). By contrast, the product in the K system presented the same characteristic reflections as the original biotite. In the Ca and Mg systems, vermiculite appeared in the products at 30 d, with basal spacings of 1.47 and 1.41 nm, respectively, attributed to the larger hydration radius of Ca^{2+} than Mg^{2+} (Ikeda *et al.*, 2007). Besides, the reflections of chlorite were observed in the XRD pattern of the products in the latter system. For the Al system, the XRD pattern of the products revealed characteristic reflections of kaolinite including (001), (020), (-110), (-1-11), and (002) planes (He *et al.*, 2017). Additionally, the interlayer space of 1.20 nm could be derived from a small amount of hydrobiotite in the products.

Subsequently, the reaction time was extended to 90 d. The XRD pattern of Bt-H-90d from the blank system showed the typical reflections of kaolinite and hydrobiotite (Fig. 2b and Fig. S1), indicating the transformation of biotite to kaolinite. Besides the prominent

https://doi.org/10.1180/mgm.2024.67 Published online by Cambridge University Press

(001) and (002) reflections, kaolinite also exhibited some relatively faint ones within the 2θ range of 20-22°, suggesting weak crystallization. In the Na, K, Mg, and Ca systems, the phase types of the 90-d products were similar to those of the 30-d products. Specifically, the XRD pattern of the Na system's product exhibited a discernible rise in the intensity of the reflection associated with a *d*-spacing of ~1.20 nm over time (Fig. 2b). This phenomenon was attributed to greater penetration of hydrated Na^+ into the biotite interlayers (i.e., the formation of more Na-containing biotite). In the Al system, with the reaction time extended from 30 to 90 days, the reflections of kaolinite in the products were further strengthened, and the splitting of (020), (-110), and (-1-11) reflections within the 2θ range of 20-22° became more pronounced, indicating an increase in the crystallinity of kaolinite (Hinckley, 1962). The above results demonstrated that compared with the blank system, Na^+, Mg^{2+}, and Ca^{2+} could promote the interlayer ion exchange of biotite but inhibit its transformation from biotite to kaolinite; while K^+ suppressed the dissolution and transformation of biotite, and Al^{3+} significantly accelerated the process.

TG/DTG analysis

The effect of cation types on the transformation products from biotite was further investigated *via* the TG analysis. The TG/DTG results showed that the original Bt exhibited no prominent DTG peak up to 1000°C because of the lack of adsorbed water and interlayer water in biotite (Fig. 3a). while the products Bt-H-30d from the blank system displayed two DTG peaks at 92 and 384°C (Fig. 3b), which were associated with the elimination of interlayer water in clay minerals (*e.g.*, hydrobiotite and vermiculite) and the dehydroxylation of polyhydroxy aluminum cations, respectively (Perez-Rodriguez *et al.*, 2011; Chen *et al.*, 2017). By contrast, the dehydration temperature (88°C) and the area of

https://doi.org/10.1180/mgm.2024.67 Published online by Cambridge University Press

the dehydration peak of interlayer water in the products Bt-Na-30d from the Na system decreased (Fig. 3c). In the blank system, the interlayer cations in the products were mainly metal ions (*e.g.*, Mg^{2+}, Al^{3+}, and Fe^{3+}) dissolved from the biotite layers, with a higher charge-to-radius ratio than Na^{+} (Table S1). These cations exerted a stronger electrostatic attraction to ligand water, thus leading to a higher dehydration temperature of interlayer water. Compared with Na^{+}, the higher hydration enthalpies made these cations more prone to form hydrated ions (Tansel, 2012), bringing more water molecules into the interlayers of biotite, thus leading to greater interlayer water loss. Additionally, Bt-Na-30d showed a larger area of the dehydroxylation peak of polyhydroxy aluminum cations than Bt-H-30d, which could be attributed to more polyhydroxy aluminum cations formed resulting from more intense dissolution of the biotite layers in the Na system. The TG/DTG curve of Bt-K-30d in the K system, similar to that of the original Bt, displayed no significant weight loss up to 1000°C (Fig. 3d), reflecting the inhibitory impact of K^{+} on the dissolution/transformation of biotite.

Unlike the Na system, the products in the Ca and Mg systems exhibited a bimodal peak pattern in interlayer water loss in the DTG curves (Fig. 3e and f), with the dehydration temperature in the Mg system (104 and 199°C) higher than in the Ca system (77 and 154°C), owing to the higher charge-to-radius ratio of Mg^{2+} (Tansel, 2012). As previously discussed, the higher the hydration enthalpy of the metal cation, the more water molecules it carried into the interlayers, theoretically resulting in a greater amount of interlayer water loss. However, the larger hydration enthalpy of Mg^{2+} led to less interlayer water loss in the Mg system (5.78% *vs*. 9.45% in the Ca system). This was because the amount of water loss from clay minerals was also related to the exchange capacity of different cations. Clay

https://doi.org/10.1180/mgm.2024.67 Published online by Cambridge University Press

minerals typically exhibited a stronger affinity for cations with larger ionic radii (Bergaya and Lagaly, 2013; Zhu *et al.*, 2016), and the larger Ca^{2+} was more likely to enter the interlayer of clay minerals through an ion exchange reaction, resulting in a larger dehydration amount of the product in the Ca system. In the DTG curve of Bt-Na-30d from the Mg system, a DTG peak at 542°C was assigned to the dehydroxylation of magnesium-oxygen/hydroxide octahedron in chlorite (Okada *et al.*, 2005), demonstrating the formation of chlorite in this system, consistent with the XRD results (Fig. 2a). It was worth noting that a broad DTG peak appeared around 800°C in the DTG curves of the products from the blank, Na, Mg, and Ca systems, probably due to the vermiculite dehydroxylation (Marcos *et al.*, 2009; Ma *et al.*, 2021; Wang *et al.*, 2022). For the Al system products, three DTG peaks at 108, 380, and 480°C were indicative of the removal of adsorbed/interlayer water, dehydroxylation of polyhydroxy aluminum cations, and dehydroxylation of kaolinite, respectively (Huertas *et al.*, 1999). The TG/DTG results confirmed the substantial impact of cation types on the phase composition of the transformation products from biotite.

FTIR analysis

The FTIR spectra of the products from biotite at 30 d in different cation systems were collected (Fig. 4 and Table S4). The products in the K system exhibited similar vibration absorption bands to the original Bt, including the stretching vibration of interlayer water (3445 cm^{-1}), Si–O stretching vibration (1001 cm^{-1} for the strong absorption region, 707 and 684 cm^{-1} for the weak absorption regions), and Si–O bending vibration (462 cm^{-1}) (Madejová *et al.*, 2017). Compared to the above two systems, the area of the stretching vibration band of interlayer water increased in the blank, Na, Mg, and Ca systems, and the increase followed the order Bt-Ca-30d > Bt-Mg-30d/Bt-H-30d > Bt-Na-30d, which was

https://doi.org/10.1180/mgm.2024.67 Published online by Cambridge University Press

consistent with the TG/DTG results. A pronounced shoulder absorption at 3561 cm^{-1} appeared in the FTIR spectrum of the product from the Mg system, derived from the Mg-OH stretching vibration of chlorite (Madejová *et al.*, 2017). The Si–O stretching vibration absorption bands in the mid-frequency region of the products from the above four systems were blue-shifted (1006-1011 cm^{-1}) and narrowed compared to the original Bt (Fig. 4). This change could be attributed to the reduced Al substitution for Si resulting from the dissolution of Al from the tetrahedra. Moreover, besides the Si–O bending vibration absorption band of the original biotite (~462 cm^{-1}) in the low-frequency region, a weaker shoulder absorption appeared on the high-frequency side of this band for these four products, implying that the current transformation product belonged to a transition phase from trioctahedral to dioctahedral minerals.

Compared to the above systems, the FTIR spectrum of the product from the Al system exhibited the characteristic infrared vibrations of kaolinite, including the structural Al–OH stretching vibrations in the high-frequency region (3698, 3670, 3649, 3620 cm^{-1}), Si–O stretching vibrations (1109, 1033, 1007 cm^{-1}) and Al–OH bending vibration (913 cm^{-1}) in the mid-frequency region, as well as the Si–O–Si(Al^{VI}) stretching vibrations (790, 754, 699 cm^{-1}) and Si–O bending vibrations (538, 470, 432 cm^{-1}) in the low-frequency region (Fig. 4) (Cuadros *et al.*, 2015). In particular, the Si–O bending vibration in the low-frequency region split from a single band of biotite (462 cm^{-1}) into three sharp absorption bands, indicating the complete transformation from trioctahedral to dioctahedral minerals. This result also demonstrated that the transformation rate of biotite in the Al system was relatively fast. When the reaction time was extended to 90 d, the phase types did not change significantly for the products in other systems based on the XRD patterns (Fig. 2), except

https://doi.org/10.1180/mgm.2024.67 Published online by Cambridge University Press

for the blank system. As shown in the FTIR pattern of Bt-H-90d, all the characteristic infrared vibrations of kaolinite appeared (Fig. S2), confirming the formation of kaolinite, consistent with the XRD results.

Mössbauer spectra analysis

Mössbauer spectra analysis, an important structural analysis method, can be utilized to analyze the occupancy, valence state, and Fe^{3+}/Fe^{2+} ratio of iron within clay minerals (Yan *et al.*, 2021). Biotite has two distinct octahedral sites: the *trans*-octahedral (M1) site and the *cis*-octahedral (M2) site, with the M1 octahedron being slightly larger and less symmetrical than the M2 octahedron (Fig. 5a). The occupancy and valence state of Fe in the octahedral sites of biotite can be ascertained by examining the quadrupole splitting (QS) and isomer shift (IS) values derived from the Mössbauer spectra. The original Bt exhibited an asymmetric Mössbauer spectrum, which was fitted into three doublets, corresponding to structural Fe^{2+}_{M1}, Fe^{2+}_{M2}, and Fe^{3+}_{M1+M2} of biotite, respectively (Fig. 5b) (Cornell and Schwertmann, 2003). The fitting results indicated that the biotite sample contained approximately 63% Fe^{2+} and 37% Fe^{3+} (Table S5).

Extensive research has proven that the oxidation of structural Fe^{2+} is a pivotal process in biotite weathering, with the level of oxidation serving as an indicator of the dissolution and transformation stages of biotite (Velde and Meunier, 2008; Bray *et al.*, 2015). The Mössbauer spectra of the 90-d products from biotite in various cation systems were further measured (Fig. 5). The Mössbauer spectrum of Bt-H-90d in the blank system could be fitted into a sextet and two doublets (Fig. 5c), which were attributed to hematite, Fe^{2+}_{M1+M2} and Fe^{3+}_{M1+M2} of the clay minerals (Cornell and Schwertmann, 2003), with a higher ratio of Fe^{3+}_{M1+M2} and Fe^{2+}_{M1+M2} than that of biotite (Table S5). Bt-K-90d from the K system

https://doi.org/10.1180/mgm.2024.67 Published online by Cambridge University Press

showed a similar Mössbauer spectrum (Fig. 5d) to the original biotite (Fig. 5b), indicating that K inhibited the transformation of biotite. The Mössbauer spectra of the products from the Na, Mg, and Ca systems all revealed a sextet and two doublets upon fitting (Fig. 5e-g), similar to the blank system (Fig. 5c). However, the intensity of the sextet was much weaker than that of Bt-H-90d, due to less hematite in the cation systems. The ratios of $Fe^{3+}_{M1+M2}/Fe^{2+}_{M1+M2}$ in the clay minerals of these systems were also lower than that of the blank one (Table S5). These comparative results indicated that Na^{+}, Mg^{2+}, and Ca^{2+} inhibited the biotite transformation in the later phases of the reaction. Lemine *et al.* (2010) studied the Mössbauer spectra of nanoscale hematite and found that a decreased size of hematite would result in a smaller hyperfine magnetic field (B_{HF}). The Mössbauer parameters showed that the B_{HF} values of hematite in the products of the Na, Mg, and Ca systems decreased in sequence (Table S5), implying that the size of the hematite produced gradually decreased. Moreover, the ratios of $Fe^{3+}_{M1+M2}/Fe^{2+}_{M1+M2}$ in the clay minerals in these three systems were 4.15, 3.67, and 3.34, respectively, indicating a decrease in the content of Fe^{3+}_{M1+M2}, which suggested that the inhibitory effect of Na^{+}, Mg^{2+}, and Ca^{2+} on biotite transformation increased in sequence. As for Bt-Al-90d in the Al system, its Mössbauer spectrum was fitted into a sextet and a doublet (Fig. 6h), corresponding to hematite and Fe^{3+}_{M1+M2} of the clay mineral. Compared with the blank system, the Fe content in the clay minerals of the Al system product further decreased, while the amount of hematite increased and Fe^{2+} almost disappeared, indicating that the addition of Al^{3+} promoted the transformation of biotite.

Morphology of biotite-transformed products in various cation systems

TEM and EDS results showed that the original biotite possessed large layers with

https://doi.org/10.1180/mgm.2024.67 Published online by Cambridge University Press

relatively smooth and uniform surfaces and was rich in Si, Al, Mg, Fe, and K (Fig. S3). Following the dissolution reaction of biotite for 90 d, the product Bt-H-90d in the blank system exhibited rough edges and surfaces of the layers (Fig. 6a), due to the destruction of the biotite layers by protons. Enlarged TEM images revealed the presence of pseudo-hexagonal kaolinite layers along the edges of the large biotite layers, growing parallel to the biotite layers (Fig. 6b). Additionally, unevenly sized kaolinite particles were observed on the surface of the large layers, with a large amount of nano hematite adsorbed around (Fig. 6c). HRTEM images of the ultrathin-section samples displayed lattice fringes of ~1.20 and 1.00 nm along the *c*-axis direction (Fig. 6d). During HRTEM observation, when clay minerals containing interlayer hydrated cations were exposed to a high-energy electron beam, the interlayer water would escape, leading to layer collapse. As such, the lattice fringes of the 2:1 clay mineral along the *c*-axis direction observed in HRTEM images were generally smaller than those detected by XRD. Therefore, the lattice fringe of ~1.20 nm corresponded to vermiculite, and the observed structure in this area should be an interstratification of vermiculite and biotite, *i.e.*, hydrobiotite. Furthermore, lattice fringes measuring ~0.70 nm along the *c*-axis coexisted with hydrobiotite lattice fringes, with the former corresponding to the (001) plane of kaolinite (Fig. 6e-f). This part of the kaolinite was speculated to be formed by *in-situ* dissolution and recrystallization of Si and Al from the biotite layers (Banfield and Eggleton, 1988). The corresponding EDS pattern for this area showed a Si/Al ratio close to 1, with K essentially leached out (Fig. 6g-h), further confirming the formation of kaolinite, consistent with the XRD, FTIR, and TEM results. In the same area, small amounts of Fe and Mg were still observed, which could be attributed to partially residual hydrobiotite.

https://doi.org/10.1180/mgm.2024.67 Published online by Cambridge University Press

Compared to the products in the blank system, those in the Na, Mg, and Ca systems showed more disordered and fragmented layers (Fig. 7a-c), which may be related to the swelling and cracking of the flake layers caused by the entry of large radius hydrated cations into the interlayers of biotite. On the surface of the layers, rhombic-shaped hematite appeared, with particle size decreasing in the sequence of Na, Mg, and Ca systems, consistent with the Mössbauer spectra results (Fig. 5). Unlike the blank system, only a small amount of kaolinite was observed at the edge of the layers in the Na system product, with no observation in the Mg and Ca system products. These results further indicated that these cations inhibited the dissolution and transformation of biotite in the later stages of the reactions, with Na^+ exhibiting less inhibition than Mg^{2+} and Ca^{2+}. HRTEM image of the ultrathin-section sample of the Na system product showed a lattice fringe with a period of ~1.00 nm (Fig. 7d). Still, it could not be distinguished whether it corresponded to the original biotite or biotite with interlayer hydrated Na^+ (*i.e.*, sodium-bearing biotite), as sodium-bearing biotite lost the interlayer water under high-energy electron beam irradiation, resulting in a reduction of the interlayer spacing from 1.20 to 1.00 nm. In addition, we also observed a lattice stripe of ~1.20 nm in this sample (Fig. 7d and e), which corresponded to vermiculite, indicating that the structural ions (such as Al) dissolved from biotite entered the interlayer. TEM image of the K system product displayed that the layer structure of biotite remained relatively intact, but it was covered with more amorphous iron hydroxide aggregates (Fig. 7f). In contrast, the Al system product contained a large amount of well-crystallized pseudo-hexagonal flaky kaolinite, and the hematite particles on the surface were mostly intact rhombic, with a larger size (Fig. 7g). EDS results indicated a Si/Al ratio close to 1, with minor Fe content (Fig. S4). HRTEM image of the ultrathin-

https://doi.org/10.1180/mgm.2024.67 Published online by Cambridge University Press

section sample showed clear lattice fringes around 0.70 nm, attributed to the (001) plane of kaolinite (Fig. 7h-i), further revealing the good crystallinity of kaolinite.

Discussion on biotite dissolution and transformation mechanisms

The results above indicated that metal cations can regulate the dissolution and transformation rate of biotite and alter the transformation products, with different metal cations exhibiting different influences on the process (Fig. S5). In the blank system, the products at 30 d mainly consisted of vermiculite, chlorite, and hydrobiotite, with a substantial amount of biotite still retained. After 90 d of reaction, poorly crystalline kaolinite appeared along with nano hematite aggregates on its surface. The addition of K^+ significantly inhibited the dissolution and transformation of biotite. In the K system, biotite remained the main phase of the products even following the reaction for 90 d, although protons could still attack the layer edges, leading to the aggregation of dissolved Fe on the biotite surface to form amorphous iron hydroxides. Na^+, Mg^{2+}, and Ca^{2+} could promote the biotite dissolution but inhibit its transformation into kaolinite. The products in the Na system were sodium-bearing biotite, vermiculite, hematite, and a small amount of kaolinite, while the products in the Mg and Ca systems were mainly vermiculite, chlorite, and hematite. Al^{3+} generated a large number of protons through its hydrolysis, which accelerated the dissolution and transformation of biotite and consequently resulted in well-crystallized kaolinite and hematite as the products.

TEM images of the 90-d product in the blank system showed that kaolinite appeared at the edges of the biotite layers, with its (001) plane parallel to the basal plane of biotite (Fig. 6b). HRTEM images of the ultrathin-section sample revealed that the kaolinite layers and hydrobiotite layers were stacked along the *c*-axis (Fig. 6f). We also observed that

https://doi.org/10.1180/mgm.2024.67 Published online by Cambridge University Press

kaolinite grew on the surface of the precursor mineral layer in this sample (Fig. 6c). These results all indicated that the newly formed kaolinite had a similar orientation to the precursor mineral, showing a certain inheritability. Banfield and Eggleton (1988) examined natural biotite weathering samples using TEM. They observed that, unlike vermiculite, which directly inherited the structure and orientation of biotite, kaolinite grew epitaxially on existing layered silicate structures with Al and Si (from solution or amorphous precursors) to obtain a similar orientation to biotite. The dissolution-recrystallization mechanism emphasized the complete dissolution of precursor minerals followed by the gradual formation of new minerals, making it difficult for the newly formed minerals to inherit the crystal structure characteristics (Dudek *et al.*, 2006). Therefore, based on previous studies and our experimental results, the dissolution mechanism of the original biotite layers was speculated as follows: due to the slow dissolution rate, the leached elements (*e.g.*, Al and Si) did not undergo long-distance migration but were adsorbed on the surface of the altered biotite layers, forming an Al and Si supersaturated environment, and gradually crystallizing and growing epitaxially into kaolinite (Fig. S5). This dissolution-reprecipitation mechanism occurring at the mineral interface could to some extent maintain the topological structure of the original mineral (Putnis, 2014; Li *et al.*, 2019), which was manifested in this study as a similar orientation of kaolinite and biotite. In the Al system, Al^{3+} hydrolysis produced a large number of protons, accelerating the dissolution of biotite (Bickmore *et al.*, 2001). Moreover, Al in the solution combined with leached Si to form a silicon-aluminum complex (Li *et al.*, 2020), accelerating the diffusion of leached Si from the mineral surface into the solution. The rapid dissolution of biotite provided a large source of Si, which combined with Al in the solution and eventually

https://doi.org/10.1180/mgm.2024.67 Published online by Cambridge University Press

crystallized into kaolinite (Fig. S5). In this dissolution-reprecipitation process, the precursor mineral layers were completely dissolved into ions or ion clusters that easily migrated and diffused in the solution. The mineral layers were formed by recrystallization, making it difficult to maintain the orientation of the precursor minerals. The TEM image of Bt-Al-90d in the Al system showed that kaolinite was well crystallized and disordered in stacking (Fig. 7g-i), once again demonstrating the formation of kaolinite through the dissolution-recrystallization mechanism. The results indicated that metal cations altered the generation mechanism of kaolinite by changing the dissolution process of biotite.

Previous studies showed that the dissolution of clay minerals in acidic environments primarily occurred at the edges because the silicon-oxygen bonds in the basal plane were charge-saturated and highly stable (Kaviratna and Pinnavaia, 1994; Li *et al.*, 2020); in acidic solutions (pH 1.08), the rate of dissolution at the edges of biotite layers was about 250 times greater than that at the basal plane (Turpault and Trotignon, 1994). For the Na, Mg, and Ca systems, cations first entered the interlayers of biotite through ion exchange, causing internal stress that promoted the buckling and cracking of the layers (Hu *et al.*, 2013; Bray *et al.*, 2015). The development of cracks results in the formation of more edges, thus accelerating the dissolution of biotite layers. However, Na^+, Mg^{2+}, and Ca^{2+} inhibited the subsequent phase transformation. Min and Jun (2016) found that Na^+ and Ca^{2+} could hinder plagioclase ($CaAl_2Si_2O_8$) dissolution by vying with protons for adsorption on the plagioclase surface, thereby reducing the proton attack on its structure. Similarly, cations would rival protons for access to the surface and interlayer sites of biotite, inhibiting proton attacks on the layers. Therefore, we believed that the effect of cations on biotite dissolution was simultaneously constrained by the cation-K^+ exchange reaction (enhancing effect) and

https://doi.org/10.1180/mgm.2024.67 Published online by Cambridge University Press

the cation-proton competitive adsorption (inhibitory effect). During the initial phase of the reaction, a large number of protons in the solution resulted in rapid layer dissolution and the intense cationic exchange reaction led to more layer cracks, so the overall effect was that cations enhanced the dissolution of biotite. As Na^+, Mg^{2+}, and Ca^{2+} entered the interlayers, the enhancing effect gradually decreased due to diffusion limitations of the cation-K^+ exchange reaction, and as the reaction proceeded, protons were gradually consumed. In the later stages of the reaction, with fewer protons in the solution, the dissolution rate of the layers slowed down, and the inhibitory effect produced by the competition between cations and protons became dominant, leading to the inhibition of phase transformation. Due to the small ionic radii and high charges of Mg^{2+} and Ca^{2+}, the mineral (*e.g.*, biotite) surface had a stronger adsorption effect on these two cations than on Na^+ (McDonald *et al.*, 2005; Hu *et al.*, 2013). Therefore, the competition between protons and Na^+ on the mineral surface was less than the competition between protons and Mg^{2+}/Ca^{2+}, in other words, the chance of protons attacking the layers in the Mg and Ca systems was smaller, leading to a stronger inhibitory effect of Mg^{2+} and Ca^{2+} on the biotite transformation. Mössbauer spectroscopy and TEM results both well illustrated this point. Similarly, in the K system, adding K^+ prevents the outward diffusion of K^+ within the interlayers of biotite, and the competitive effect between K^+ and protons leads to a reduced proton attack on the layers, thereby inhibiting the dissolution and transformation of biotite.

Conclusion

In summary, we selected five typical metal cations (Na^+, K^+, Ca^{2+}, Mg^{2+}, Al^{3+}) as representatives to study the influence of various metal cations on the dissolution and transformation process of biotite. The results indicated that the type of metal cations could

https://doi.org/10.1180/mgm.2024.67 Published online by Cambridge University Press

significantly regulate the dissolution and transformation of biotite. Compared with the blank system, K^+ impeded the dissolution and transformation of biotite, leading to the formation of amorphous iron hydroxides on the biotite surface; Na^+, Mg^{2+}, and Ca^{2+} promoted the dissolution of biotite but inhibited its transformation into kaolinite. In the Na system, the products included sodium-bearing biotite, vermiculite, hematite, and a small amount of kaolinite; while in the Mg and Ca systems, the products primarily consisted of vermiculite, chlorite, and hematite. Al^{3+} notably accelerated the dissolution and transformation of biotite, resulting in the formation of well-crystallized kaolinite and hematite. Furthermore, metal cations could alter the dissolution rate of biotite, thereby changing the formation mechanism of kaolinite. In the blank system, the dissolution rate of biotite was slow, and the released elements such as Al and Si accumulated on the surface of biotite, growing epitaxially into kaolinite; while in the Al system, the rapid dissolution of biotite provided a large source of Si, which combined with Al in the solution to form kaolinite through a dissolution-recrystallization mechanism. In addition, the exchange reaction of metal cations with K^+ and the competitive adsorption between metal cations and protons simultaneously affected the dissolution process of biotite. This work offered a theoretical basis for a deeper comprehension of the factors influencing the weathering of silicate minerals and new insights into the evolution of clay minerals in terrestrial surface environments.

Declaration of Competing Interest

The authors declare that there are no competing financial interests.

https://doi.org/10.1180/mgm.2024.67 Published online by Cambridge University Press

Acknowledgments

This study was supported by the Key-Area Research and Development Program of Guangdong Province (2020B0101370003), National Natural Science Foundation of China (42225203, 42272045, 41921003, 41825003), Tuguangchi Award for Excellent Young Scholar GIG, CAS (TGC202302), Youth Innovation Promotion Association CAS (2020347), Natural Science Foundation for Distinguished Young Scientists of Guangdong Province (2023B1515020006), and Science and Technology Planning of Guangdong Province, China (2023B1212060048).

Supplementary material

To view supplementary material for this article, please visit https://doi.org/xxx.

References

Banfield, J.F. and Eggleton, R.A. (1988) Transmission electron microscope study of biotite weathering. *Clays and Clay Minerals*, **36**, 47-60.

Bergaya, F. and Lagaly, G. (2013) Chapter 1 - General introduction: Clays, clay minerals, and clay science. Pp. 1-19. In F. Bergaya, and G. Lagaly, Eds. *Handbook of Clay Science, 2nd ed, Developments in Clay Science*, 5, Elsevier, Amsterdam.

Bickmore, B.R., Bosbach, D., Hochella, M.F., Jr., Charlet, L. and Rufe, E. (2001) In situ atomic force microscopy study of hectorite and nontronite dissolution: Implications for phyllosilicate edge surface structures and dissolution mechanisms. *American Mineralogist*, **86**, 411-423.

Bowser, C.J. and Jones, B.F. (2002) Mineralogic controls on the composition of natural waters dominated by silicate hydrolysis. *American Journal of Science*, **302**, 582-

https://doi.org/10.1180/mgm.2024.67 Published online by Cambridge University Press

662.

Bray, A.W., Oelkers, E.H., Bonneville, S., Wolff-Boenisch, D., Potts, N.J., Fones, G. and Benning, L.G. (2015) The effect of pH, grain size, and organic ligands on biotite weathering rates. *Geochimica et Cosmochimica Acta*, **164**, 127-145.

Breen, K.J., Angelo, C.G., Masters, R.W. and Sedam, A.C. (1985) US geological survey: Water resources investigation report (84-4314). *Ohio Department of Natural Resources, Division of Oil and Gas (Columbus, OH)*.

Cappelli, C., Van Driessche, A.E.S., Cama, J. and Huertas, F.J. (2023) Alteration of trioctahedral micas in the presence of inorganic and organic acids. *Applied Clay Science*, **238**, 106923.

Carlson, L. and Schwertmann, U. (1981) Natural ferrihydrites in surface deposits from finland and their association with silica. *Geochimica et Cosmochimica Acta*, **45**, 421-429.

Chen, Q.Z., Zhu, R.L., Ma, L.Y., Zhou, Q., Zhu, J.X. and He, H.P. (2017) Influence of interlayer species on the thermal characteristics of montmorillonite. *Applied Clay Science*, **135**, 129-135.

Cho, Y. and Komarneni, S. (2007) Synthesis of kaolinite from micas and K-depleted micas. *Clays and Clay Minerals*, **55**, 565-571.

Cornell, R.M. and Schwertmann, U. (2003) *The Iron Oxides: Structure, Properties, Reactions, Occurrences and Uses*. John Wiley & Sons.

Cuadros, J., Vega, R. and Toscano, A. (2015) Mid-infrared features of kaolinite-dickite. *Clays and Clay Minerals*, **63**, 73-84.

Dudek, T., Cuadros, J. and Fiore, S. (2006) Interstratified kaolinite-smectite: Nature of the

https://doi.org/10.1180/mgm.2024.67 Published online by Cambridge University Press

layers and mechanism of smectite kaolinization. *American Mineralogist*, **91**, 159-170.

Galán, E. and Ferrell, R.E. (2013) Chapter 3 - Genesis of clay minerals. Pp. 83-126. In F. Bergaya, and G. Lagaly, Eds. *Handbook of Clay Science, 2nd ed, Developments in Clay Science*, 5, Elsevier, Amsterdam.

Ganor, J., Reznik, I.J. and Rosenberg, Y.O. (2009) Organics in water-rock interactions. *Reviews in Mineralogy and Geochemistry*, **70**, 259-369.

Haward, S.J., Smits, M.M., Ragnarsdóttir, K.V., Leake, J.R., Banwart, S.A. and McMaster, T.J. (2011) In situ atomic force microscopy measurements of biotite basal plane reactivity in the presence of oxalic acid. *Geochimica et Cosmochimica Acta*, **75**, 6870-6881.

He, H.P., Ji, S.C., Tao, Q., Zhu, J.X., Chen, T.H., Liang, X.L., Li, Z.H. and Dong, H.L. (2017) Transformation of halloysite and kaolinite into beidellite under hydrothermal condition. *American Mineralogist*, **102**, 997-1005.

Hiemstra, T. (2018) Ferrihydrite interaction with silicate and competing oxyanions: Geometry and hydrogen bonding of surface species. *Geochimica et Cosmochimica Acta*, **238**, 453-476.

Hinckley, D.N. (1962) Variability in "crystallinity" values among the kaolin deposits of the coastal plain of Georgia and South Carolina. *Clays and Clay Minerals*, **11**, 229-235.

Holgersson, S., Drake, H., Karlsson, A. and Krall, L. (2024) Biotite dissolution kinetics at pH 4 and 6.5 under anaerobic conditions and the release of dissolved Fe(II). *Chemical Geology*, **662**, 122204.

Hu, Y., Ray, J.R. and Jun, Y.-S. (2011) Biotite-brine interactions under acidic hydrothermal

https://doi.org/10.1180/mgm.2024.67 Published online by Cambridge University Press

conditions: Fibrous illite, goethite, and kaolinite formation and biotite surface cracking. *Environmental Science & Technology*, **45**, 6175-6180.

Hu, Y., Ray, J.R. and Jun, Y.-S. (2013) Na^{+}, Ca^{2+}, and Mg^{2+} in brines affect supercritical CO_2–brine–biotite interactions: Ion exchange, biotite dissolution, and illite precipitation. *Environmental Science & Technology*, **47**, 191-197.

Huertas, F.J., Fiore, S., Huertas, F. and Linares, J. (1999) Experimental study of the hydrothermal formation of kaolinite. *Chemical Geology*, **156**, 171-190.

Ikeda, T., Boero, M. and Terakura, K. (2007) Hydration properties of magnesium and calcium ions from constrained first principles molecular dynamics. *The Journal of Chemical Physics*, **127**, 074503.

Jeong, G.Y. and Kim, H.B. (2003) Mineralogy, chemistry, and formation of oxidized biotite in the weathering profile of granitic rocks. *American Mineralogist*, **88**, 352-364.

Jolicoeur, S., Ildefonse, P. and Bouchard, M. (2000) Kaolinite and gibbsite weathering of biotite within saprolites and soils of central Virginia. *Soil Science Society of America Journal*, **64**, 1118-1129.

Kalinowski, B.E. and Schweda, P. (1996) Kinetics of muscovite, phlogopite, and biotite dissolution and alteration at pH 1-4, room temperature. *Geochimica et Cosmochimica Acta*, **60**, 367-385.

Kaviratna, H. and Pinnavaia, T.J. (1994) Acid hydrolysis of octahedral Mg^{2+} sites in 2:1 layered silicates: An assessment of edge attack and gallery access mechanisms. *Clays and Clay Minerals*, **42**, 717-723.

Kharaka, Y.K. and Hanor, J.S. (2014) 7.14 - Deep fluids in sedimentary basins. Pp. 471-515. In H.D. Holland, and K.K. Turekian, Eds. *Treatise on Geochemistry, 2nd ed,*

https://doi.org/10.1180/mgm.2024.67 Published online by Cambridge University Press

Elsevier, Oxford.

Kim, J.-Y. and Kim, Y. (2015) Sorption of cesium on weathered biotite: The effects of cations in solution. *Catena*, **135**, 107-113.

Lamarca-Irisarri, D., Van Driessche, A.E.S., Jordan, G., Cappelli, C. and Huertas, F.J. (2019) The role of pH, temperature, and NH_4^+ during mica weathering. *ACS Earth and Space Chemistry*, **3**, 2613-2622.

Lemine, O.M., Sajieddine, M., Bououdina, M., Msalam, R., Mufti, S. and Alyamani, A. (2010) Rietveld analysis and Mössbauer spectroscopy studies of nanocrystalline hematite α-Fe_2O_3. *Journal of Alloys and Compounds*, **502**, 279-282.

Li, S.Y., He, H.P., Tao, Q., Xi, Y.F., Chen, A.Q., Ji, S.C., Zhang, C.Q., Yang, Y.P. and Zhu, J.X. (2019) Transformation of boehmite into 2:1 type layered aluminosilicates with different layer charges under hydrothermal conditions. *Applied Clay Science*, **181**, 105207.

Li, S.Y., He, H.P., Tao, Q., Zhu, J.X., Tan, W., Ji, S.C., Yang, Y.P. and Zhang, C.Q. (2020) Kaolinization of 2:1 type clay minerals with different swelling properties. *American Mineralogist*, **105**, 687-696.

Ma, T., Sun, H., Peng, T. and Zhang, Q. (2021) Transformation process from phlogopite to vermiculite under hydrothermal conditions. *Applied Clay Science*, **208**, 106094.

Madejová, J., Gates, W.P. and Petit, S. (2017) Chapter 5 - IR spectra of clay minerals. Pp. 107-149. In W.P. Gates, J.T. Kloprogge, J. Madejová, and F. Bergaya, Eds. *Infrared and Raman Spectroscopies of Clay Minerals, Developments in Clay Science*, 8, Elsevier, Amsterdam.

Marcos, C., Arango, Y.C. and Rodriguez, I. (2009) X-ray diffraction studies of the thermal

https://doi.org/10.1180/mgm.2024.67 Published online by Cambridge University Press

behaviour of commercial vermiculites. *Applied Clay Science*, **42**, 368-378.

Masson, D., Robin, V., Joussein, E., Tertre, E. and Baron, F. (2024) Role of the crystal chemistry on the dissolution kinetics of Fe(III)-rich smectites. *Geochimica et Cosmochimica Acta*, **371**, 162-172.

McDonald, L.M., Evangelou, V.P. and Chappell, M.A. (2005) Cation exchange. Pp. 183. In D. Hillel, Ed. *Encyclopedia of Soils in the Environment*, Elsevier, Oxford.

McMaster, T.J., Smits, M.M., Haward, S.J., Leake, J.R., Banwart, S. and Ragnarsdottir, K.V. (2008) High-resolution imaging of biotite dissolution and measurement of activation energy. *Mineralogical Magazine*, **72**, 115-120.

Min, Y. and Jun, Y.-S. (2016) Anorthite dissolution under conditions relevant to subsurface CO_2 injection: Effects of Na^+, Ca^{2+}, and Al^{3+}. *Environmental Science & Technology*, **50**, 11377-11385.

Min, Y., Kim, D. and Jun, Y.-S. (2018) Effects of Na^+ and K^+ exchange in interlayers on biotite dissolution under high-temperature and high-CO_2-pressure conditions. *Environmental Science & Technology*, **52**, 13638-13646.

Nesbitt, H.W. and Young, G.M. (1984) Prediction of some weathering trends of plutonic and volcanic rocks based on thermodynamic and kinetic considerations. *Geochimica et Cosmochimica Acta*, **48**, 1523-1534.

Okada, K., Arimitsu, N., Kameshima, Y., Nakajima, A. and MacKenzie, K.J.D. (2005) Preparation of porous silica from chlorite by selective acid leaching. *Applied Clay Science*, **30**, 116-124.

Pachana, K., Zuddas, P. and Censi, P. (2012) Influence of pH and temperature on the early stage of mica alteration. *Applied Geochemistry*, **27**, 1738-1744.

https://doi.org/10.1180/mgm.2024.67 Published online by Cambridge University Press

Perez-Rodriguez, J.L., Maqueda, C., Murafa, N., Šubrt, J., Balek, V., Pulišová, P. and Lančok, A. (2011) Study of ground and unground leached vermiculite II. Thermal behaviour of ground acid-treated vermiculite. *Applied Clay Science*, **51**, 274-282.

Putnis, A. (2014) Why mineral interfaces matter. *Science*, **343**, 1441.

Samantray, J., Anand, A., Dash, B., Ghosh, M.K. and Behera, A.K. (2022) Silicate minerals - Potential source of potash - A review. *Minerals Engineering*, **179**, 107463.

Sánchez-Pastor, N., Aldushin, K., Jordan, G. and Schmahl, W.W. (2010) K^+-Na^+ exchange in phlogopite on the scale of a single layer. *Geochimica et Cosmochimica Acta*, **74**, 1954-1962.

Tamrat, W.Z., Rose, J., Grauby, O., Doelsch, E., Levard, C., Chaurand, P. and Basile-Doelsch, I. (2018) Composition and molecular scale structure of nanophases formed by precipitation of biotite weathering products. *Geochimica et Cosmochimica Acta*, **229**, 53-64.

Tansel, B. (2012) Significance of thermodynamic and physical characteristics on permeation of ions during membrane separation: Hydrated radius, hydration free energy and viscous effects. *Separation and Purification Technology*, **86**, 119-126.

Teppen, B.J. and Miller, D.M. (2006) Hydration energy determines isovalent cation exchange selectivity by clay minerals. *Soil Science Society of America Journal*, **70**, 31-40.

Turpault, M.P. and Trotignon, L. (1994) The dissolution of biotite single crystals in dilute HNO_3 at 24°C: Evidence of an anisotropic corrosion process of micas in acidic solutions. *Geochimica et Cosmochimica Acta*, **58**, 2761-2775.

Van Der Kellen, I., Derrien, D., Ghanbaja, J. and Turpault, M.-P. (2022) Recent weathering

https://doi.org/10.1180/mgm.2024.67 Published online by Cambridge University Press

promotes C storage inside large phyllosilicate particles in forest soil. *Geochimica et Cosmochimica Acta*, **318**, 328-351.

Velde, B.B. and Meunier, A. (2008) *The Origin of Clay Minerals in Soils and Weathered Rocks*. Springer Science & Business Media.

Wang, J.J., Nurdiana, A., Sato, Y., Watanabe, N. and Tsuchiya, N. (2024) Characteristics of congruent dissolution of silicate minerals enhanced by chelating ligand under ambient conditions. *American Mineralogist*, **109**, 1096-1105.

Wang, S., Gainey, L., Marinelli, J., Deer, B., Wang, X.D., Mackinnon, I.D.R. and Xi, Y.F. (2022) Effects of vermiculite on in-situ thermal behaviour, microstructure, physical and mechanical properties of fired clay bricks. *Construction and Building Materials*, 316, 125828.

Wang, W., Shi, L.P., Wu, H.Y., Ding, Z., Liang, J.J., Li, P. and Fan, Q.H. (2023) Interactions between micaceous minerals weathering and cesium adsorption. *Water Research*, **238**, 119918.

Wilson, M.J. (2004) Weathering of the primary rock-forming minerals: Processes, products and rates. *Clay Minerals*, **39**, 233-266.

Wu, Z., Chen, Y., Wang, Y., Xu, Y., Lin, Z., Liang, X. and Cheng, H. (2023) Review of rare earth element (REE) adsorption on and desorption from clay minerals: Application to formation and mining of ion-adsorption REE deposits. *Ore Geology Reviews*, **157**, 105446.

Yan, L.X., Chen, Q.Z., Yang, Y.X. and Zhu, R.L. (2021) The significant role of montmorillonite on the formation of hematite nanoparticles from ferrihydrite under heat treatment. *Applied Clay Science*, **202**, 105962.

https://doi.org/10.1180/mgm.2024.67 Published online by Cambridge University Press

Zhu, R.L., Chen, Q.Z., Zhou, Q., Xi, Y.F., Zhu, J.X. and He, H.P. (2016) Adsorbents based on montmorillonite for contaminant removal from water: A review. *Applied Clay Science*, **123**, 239-258.

https://doi.org/10.1180/mgm.2024.67 Published online by Cambridge University Press

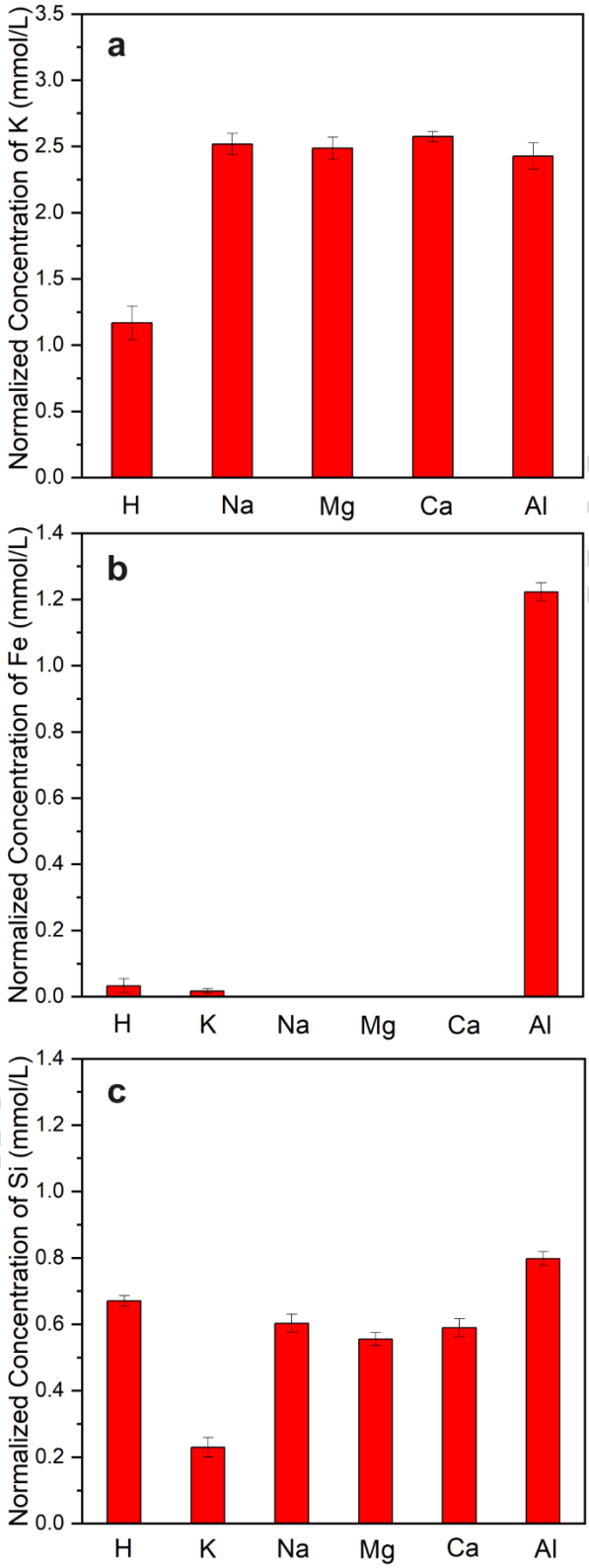

Figure 1. Normalized ion concentrations of K (a), Fe (b), and Si (c) in the supernatant of different cation systems after biotite dissolution for 30 d.

https://doi.org/10.1180/mgm.2024.67 Published online by Cambridge University Press

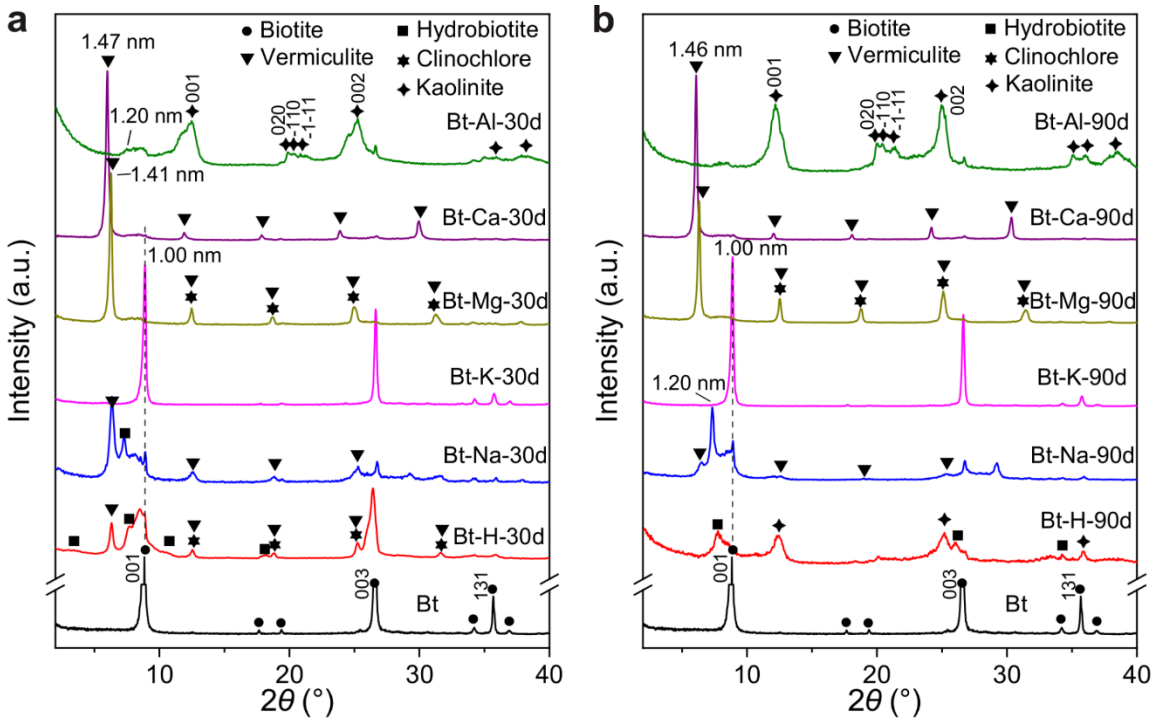

Figure 2. XRD patterns of the products from biotite in different cation systems after 30 d (a) and 90 d (b).

https://doi.org/10.1180/mgm.2024.67 Published online by Cambridge University Press

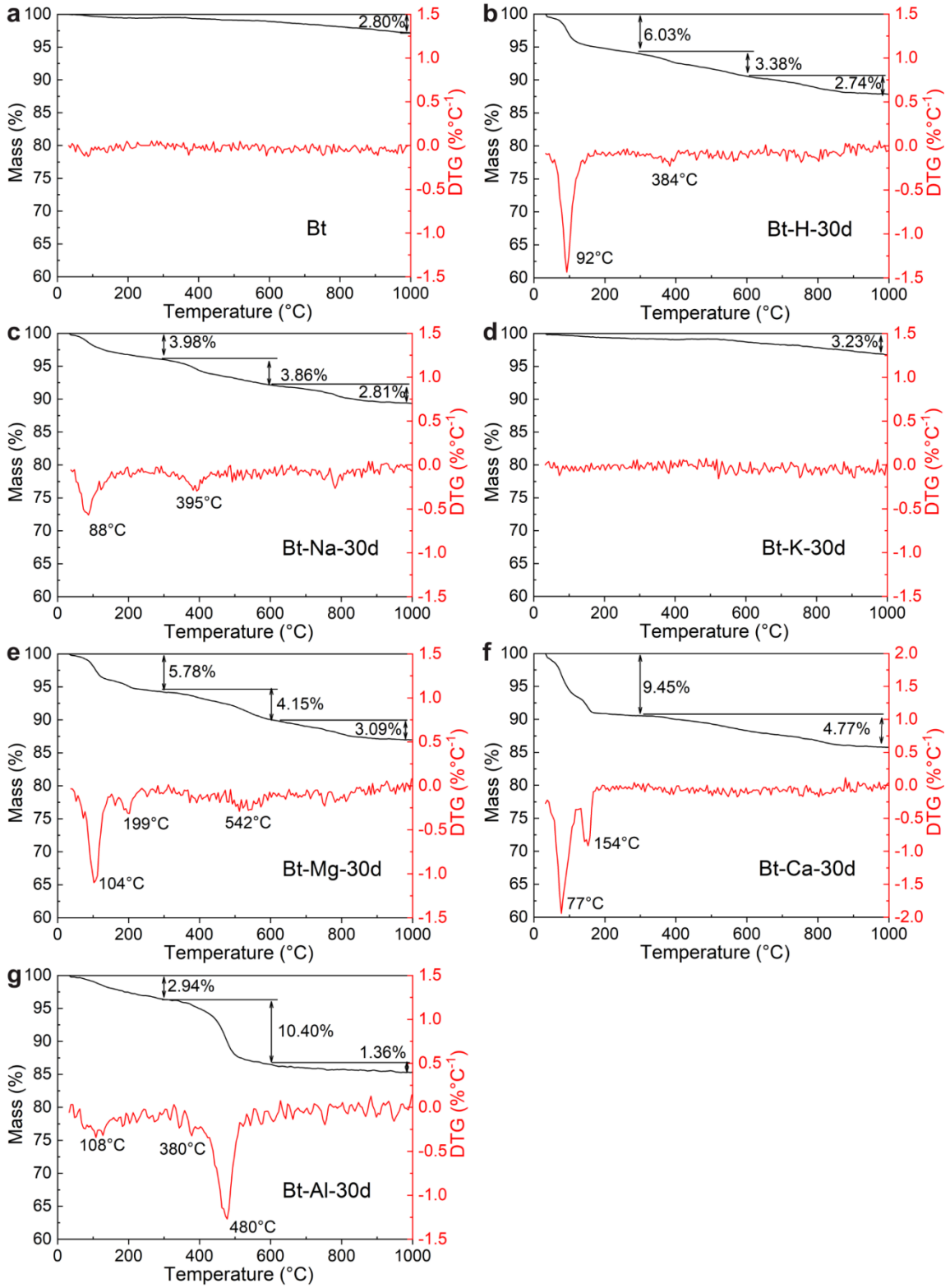

Figure 3. TG/DTG curves of the original biotite (a) and the products from biotite in different cation systems after 30 d (b-g).

https://doi.org/10.1180/mgm.2024.67 Published online by Cambridge University Press

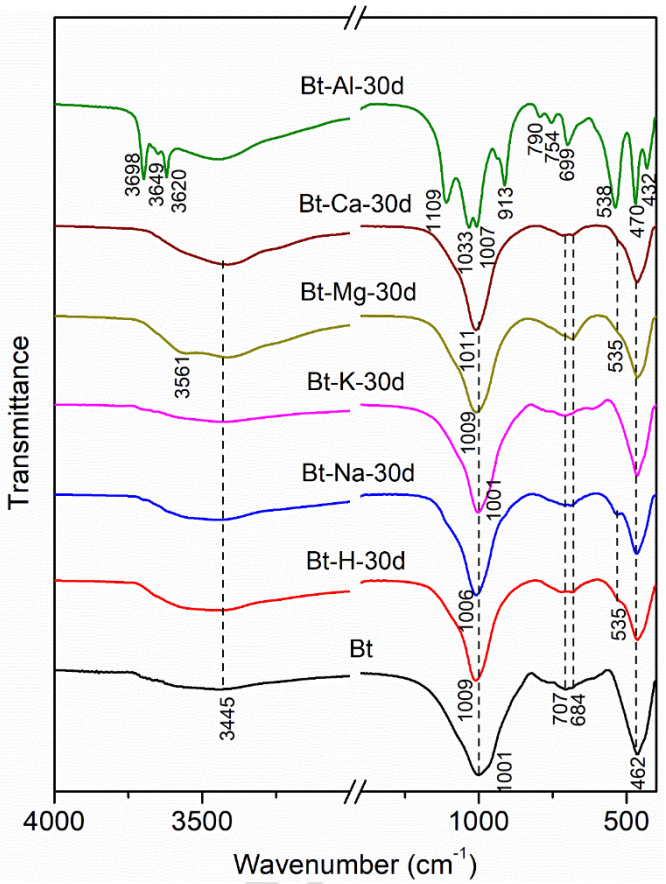

Figure 4. FTIR spectra of the products from biotite in different cation systems after 30 d.

https://doi.org/10.1180/mgm.2024.67 Published online by Cambridge University Press

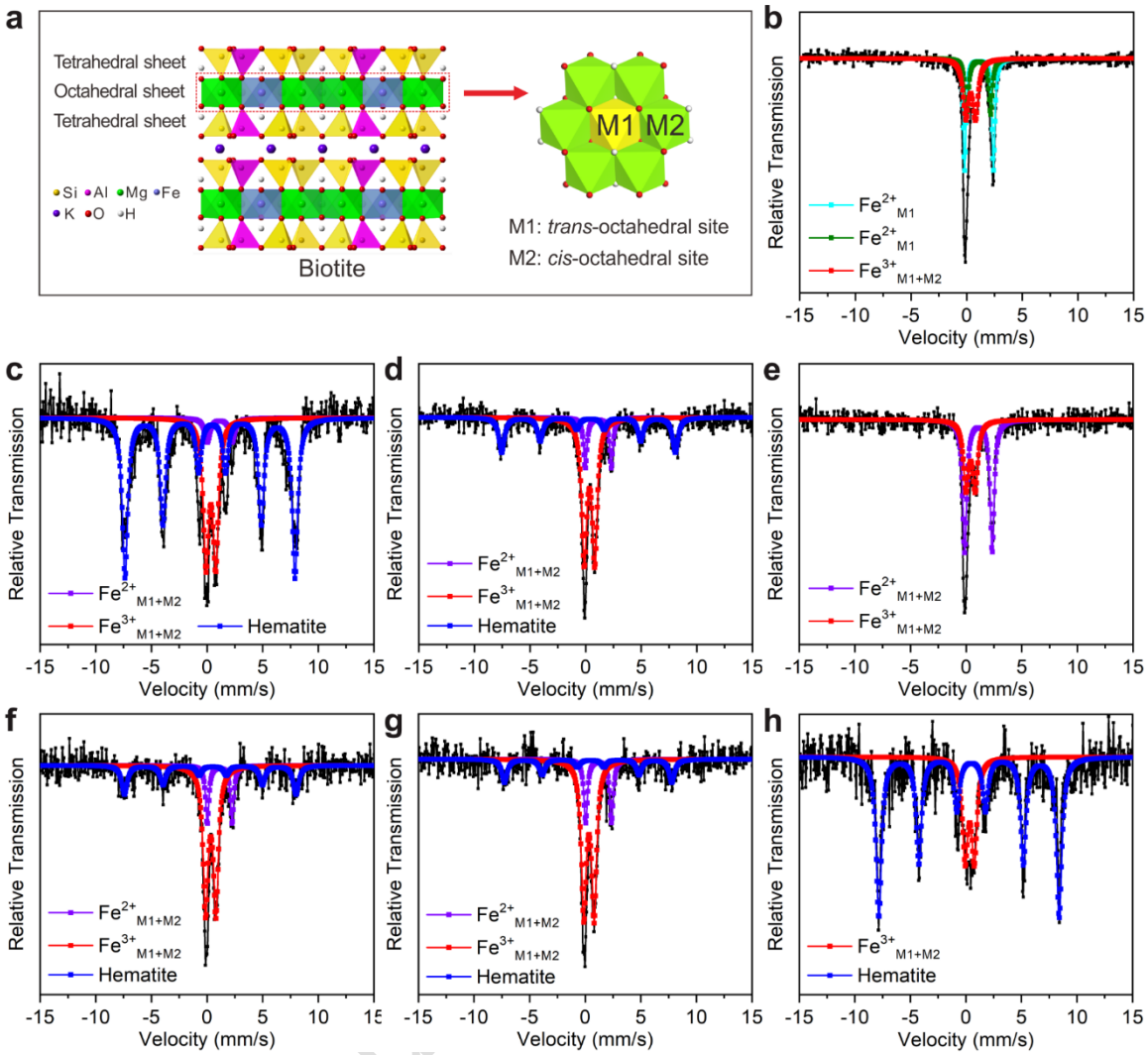

Figure 5. (a) Structure diagram of the biotite showing two distinct octahedral sites M1 and M2. Mössbauer spectra of raw biotite and the products from biotite in different cation systems after 90 d recorded at room temperature: (b) Bt, (c) Bt-H-90d, (d) Bt-K-90d, (e) Bt-Na-90d, (f) Bt-Mg-90d, (g) Bt-Ca-90d, and (h) Bt-Al-90d.

https://doi.org/10.1180/mgm.2024.67 Published online by Cambridge University Press

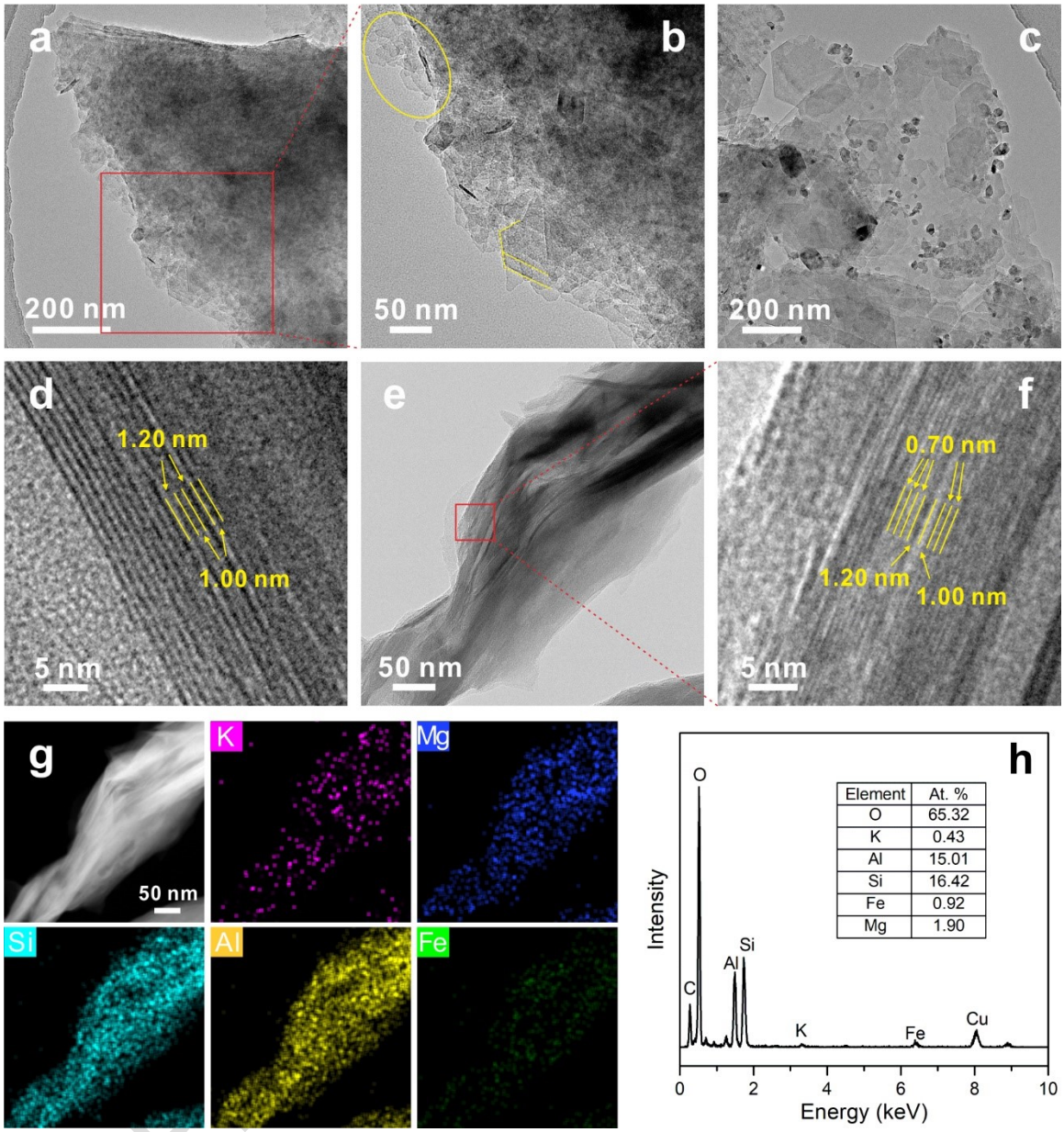

Figure 6. The morphology and composition of Bt-H-90d. (a-c) TEM images of the powdered sample; TEM images (d-f), HAADF image and EDS mapping (g), and EDS pattern (h) of the ultrathin-section specimen.

https://doi.org/10.1180/mgm.2024.67 Published online by Cambridge University Press

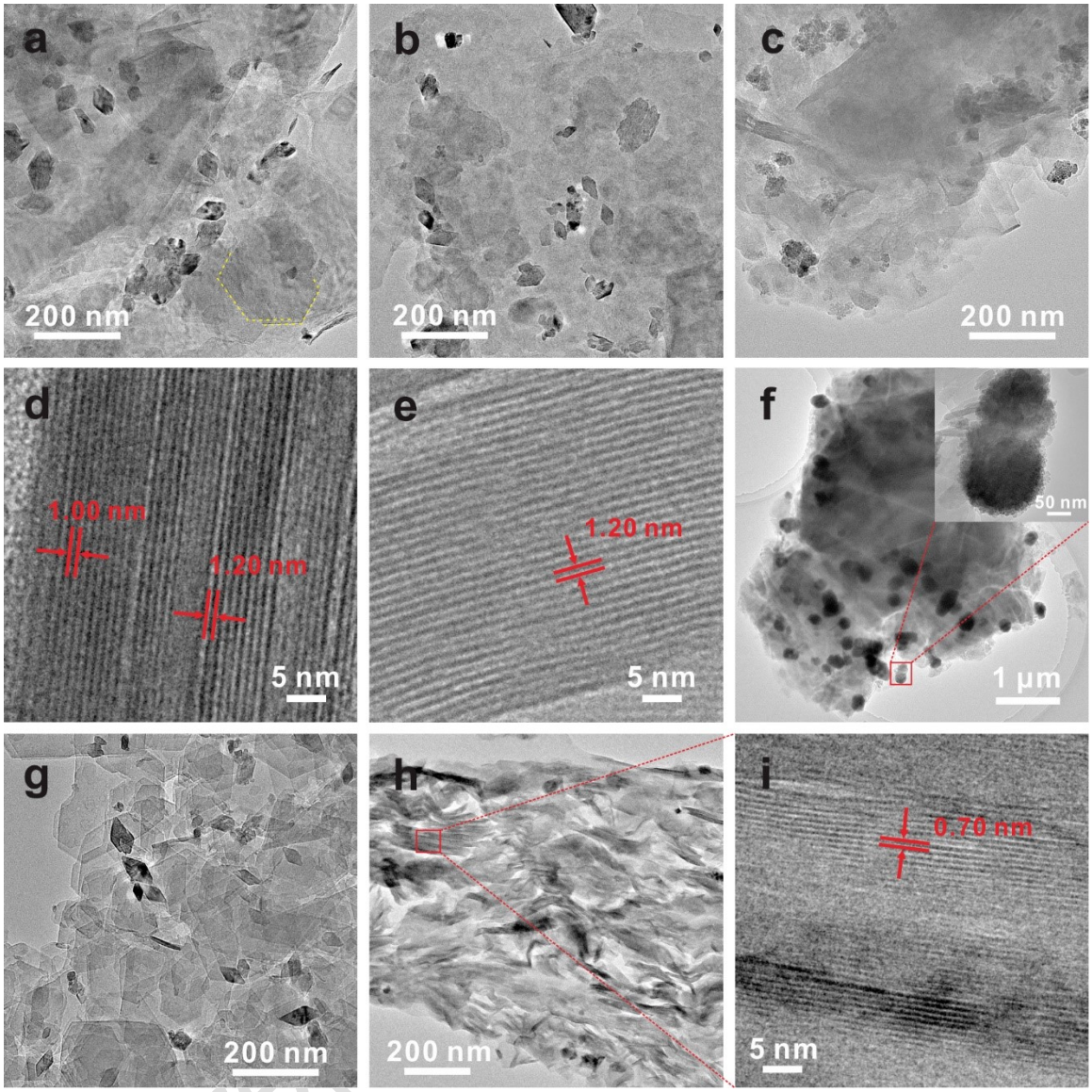

Figure 7. The morphology of the products from biotite in different cation systems after 90 d. TEM image of Bt-Na-90d (a), Bt-Mg-90d (b), Bt-Ca-90d (c), and Bt-K-90d (f); HRTEM images (of the specimen prepared via ultrathin-section method) of Bt-Na-90d (d-e); TEM image (g) and HRTEM images (of the specimen prepared via ultrathin-section method) (h-i) of Bt-Al-90d.

https://doi.org/10.1180/mgm.2024.67 Published online by Cambridge University Press